Corona wind and heat transfer

Vaessen, P.T.M.

Award date:
1985

AFDELING DER ELEKTROTECHNIEK

Vakgroep Technieken van de Energievoorziening (EHO)

Corona Wind and Heat Transfer

EH.85.A84

P.T.M. Vaessen

Afstudeerwerk verricht o.l.v.
Prof. Dr. Ir. P.C.T. van der Laan
mei 1985

T E C H N I S C H E H O G E S C H O O L E I N D H O V E N

ABSTRACT.

The convective heat transfer to or from a solid, can be significantly enhanced by a nearby corona discharge, through the interaction of the corona wind with the thermal boundary layer. Experimental measurements have been performed to investigate the character of the corona wind. Techniques used are: hot-wire anemometry and visualization with artificial mist. A comparison between corona wind and wind originating from an orifice shows that the heat transfer enhancement by corona wind is surprisingly effective because the corona wind flows as a quite laminar jet with a long reach and a small spread.

TABLE OF PHYSICAL CONSTANTS

Permittivity of vacuum	$\varepsilon_o = 8.854 \times 10^{-12}$ Fm^{-1}
Relative permittivity of water	$\varepsilon_r = 81$
Electronic charge	$e = 1.6 \times 10^{-19}$ As
Gravitational acceleration	$g = 9.8$ ms^{-2}
Viscosity of air (N.T.P.)	$\eta = 1.8 \times 10^{-5}$ Nm^{-2}s
Kinematic viscosity of air (N.T.P.)	$\nu = 1.5 \times 10^{-5}$ m^{2}s^{-1}
Density of air (N.T.P.)	$\rho = 1.2$ kgm^{-3}

CONTENTS

1. Introduction.

The enhancement of heat transfer across solid-gaseous interfaces by a nearby corona discharge has been known since 1899 (Chattock). In the 1960s increases of the heat transfer coefficient by about a factor four above that for natural convection were measured. This resulted in an intense research on this process throughout the world [1,2]. Nowadays several patents exist on the practical application of this phenomenon. The heat transfer augmentation process is however, not yet clearly explained. The corona wind itself, the character of the stream, the interaction of charged particles with the target object, or a combination of these factors may be responsible. The aim of this report is to find which factor or factors are responsible for the observed heat transfer enhancement. New applications of corona wind and an optimization of already existing apparatus are then possible. Throughout the report we employ S.I. units.

2. The Negative Corona Discharge.

In commercially used electric wind systems the corona discharge often has a negative polarity and is of the so called "Trichel-type". The main reason for choosing a negative instead of a positive discharge is the fact that a negative corona discharge in a point to plate or a point to rods configuration produces less ozone than a positive corona. Ozone is a poisonous gas and a powerful oxidizing agent which attacks almost all material in the surroundings of the discharge. Furthermore negative coronas in electron attaching gases burn more steadily up to currents of 30 μA per point, with a concentrated ionization region. Positive coronas in the contrary have a tendency to show streamer filaments shooting through the drift region towards the cathode at much lower currents than 30 μA. In a negative corona secondary processes at the cathode are possible, this is the reason that negative coronas burn more steadily than positive ones. The negative corona discharge of the "Trichel-type" [3] consists of a negative electrode with a small radius of curvature and a positive electrode, mainly acting as a charge collector. Figure 2.1 shows a negative point to plane configuration with some important quantities. The ionization processes take place in a very small region near the electrode which is stressed by a negative high voltage higher than the corona onset voltage.

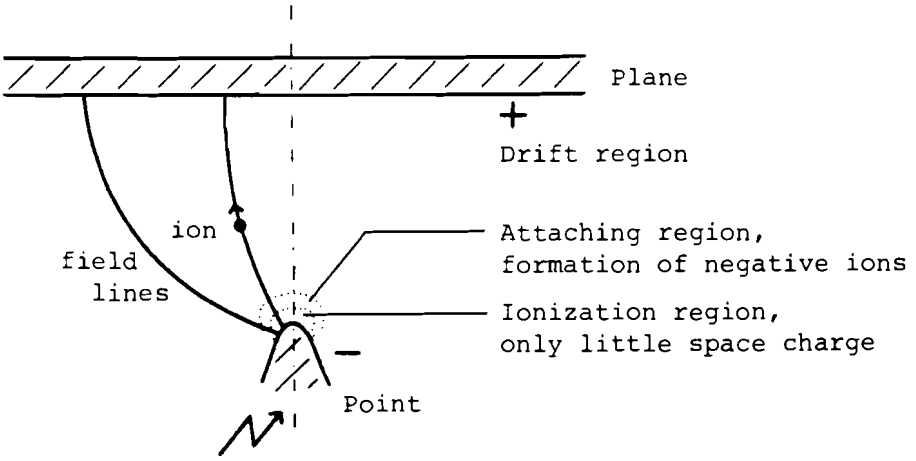

Fig. 2.1. A negative point to plane corona geometry.

If an attaching gas is present in the gap, negative ions are formed just outside the ionization region. These ions drift to the low field region near the passive positive electrode. The initial current rise caused by a Townsend electron avalanche is quenched by the accumulation of negative space charge in front of the ionization region. A new pulse can only start when this charge cloud has drifted away sufficiently far to allow the field near the cathode to rise above the onset value. The repetition frequency of these Trichel pulses can be as high as 1 MHz, so many space charge clouds may be drifting through the gap at any given time. The Trichel current pulse, i(t), waveform is independent of the average discharge current, while the repetition frequency is proportional to the average current. Figure 2.2 shows a typical Trichel pulse in air with its short rise time of about 2 ns.

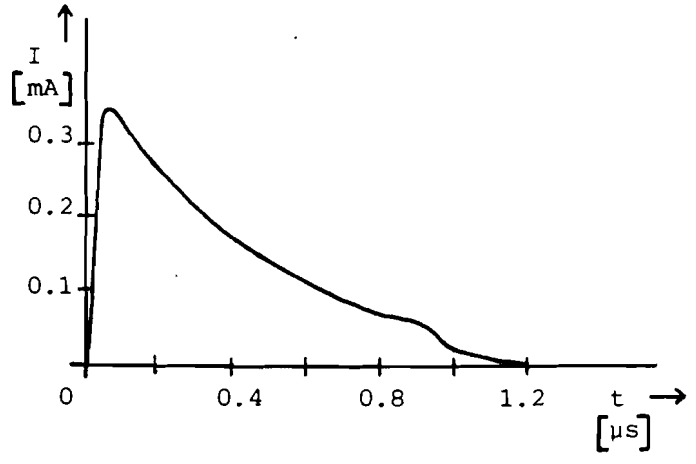

Fig. 2.2. Typical Trichel current pulse in air.

3. Corona Wind.

In a negative corona discharge in air the ionization takes place in a very small region near the electrode with the smallest radius of curvature. The rapidly drifting negative ions make frequent collisions with the neutral molecules, so that they acquire a constant drift velocity. The force caused by the electric field in the gap is then completely transferred to the neutral gas. This is the essential element in the ion drag theory [4]. The flow created in this manner is the corona wind, mostly consisting of neutral gas molecules and thus resembling jet flow. The body force,

$$\vec{F} = \rho_c \vec{E}, \qquad (3.1)$$

in which ρ_c is the charge density and $\vec{E}$ the electric field strength, is a function of the location within the jet flow and acts throughout the entire region between the electrodes. This force couples the electrical and fluid dynamical behaviour of the corona discharge and shows up as a source term in the Navier-Stokes equations [5]. The equations governing the electric, velocity and temperature field form a large set of coupled partial differential equations. The boundary conditions have a large influence on the nature of the flow field but are often difficult to formulate.

4. The Electric Wind System.

The electric wind system as shown in Fig. 4.1 consists of a flat 90° edge of 1 mm thick brass and two parallel stainless steel rods of 5 mm diameter. In this system d is the distance between the two rods and S_1 the distance between the point and the plane of the rods. In commercially used electric wind systems of this type (The METC-system, INTERPROBE Inc., Chicago) a flat plate is placed a distance h below the plane of the rods; this plate may be the heat transfer surface in an oven. We consider the point to be the center of a right handed cartesian coordinate system where the x-axis is normal to the plane of the rods. A negative high voltage is applied to the point, while the rods are grounded. The discharge is run in the Trichel-pulse regime and is operated in atmospheric air.

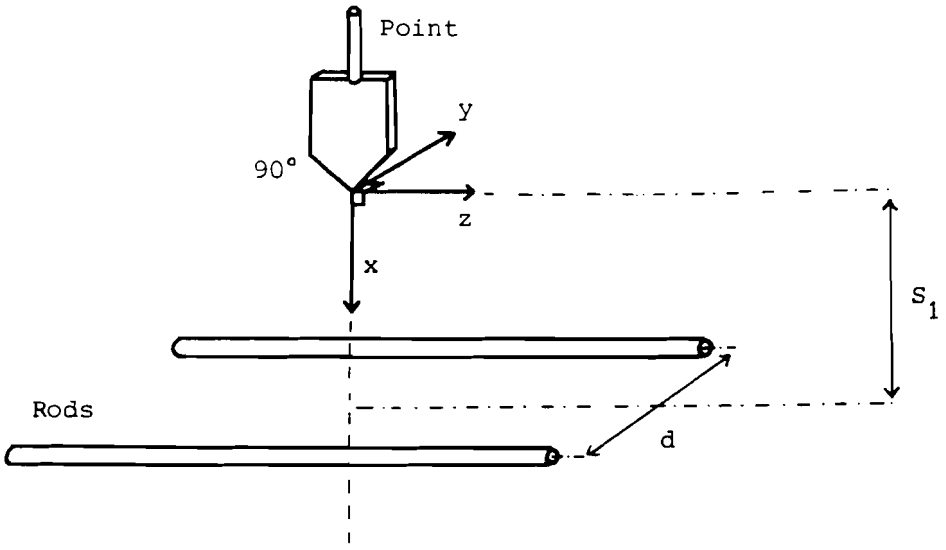

Fig. 4.1. Electric wind system.

Figure 4.2 shows the current drawn to the rods versus the voltage applied to the point. The voltage current characteristic follows the well known empirical formula [6]:

$$I_1 = K_1 V(V-V_i). \qquad (4.1)$$

I_1 is the current to the rods, V is the voltage applied to the point, V_i is the corona onset voltage and K_1 is a constant with dimensions AV^{-2}. When a grounded heat transfer plate is placed some distance below the rods and the current, I_2, drawn to this surface is measured we observe that [7]:

$$I_2 << I_1 \qquad (4.2)$$

and

$$I_2 = K_2(V-V_i). \qquad (4.3)$$

K_2 is a constant with dimensions AV^{-1}. The current I_2 is small which indicates that almost all ions reach the grounded rods. This is also confirmed by the hot-wire anemometry measurements. The values for K_1 and K_2 found from Fig. 4.2 are $K_1 = 1.8 \times 10^{-13}$ AV^{-2} and $K_2 = 1.5 \times 10^{-10}$ AV^{-1}.

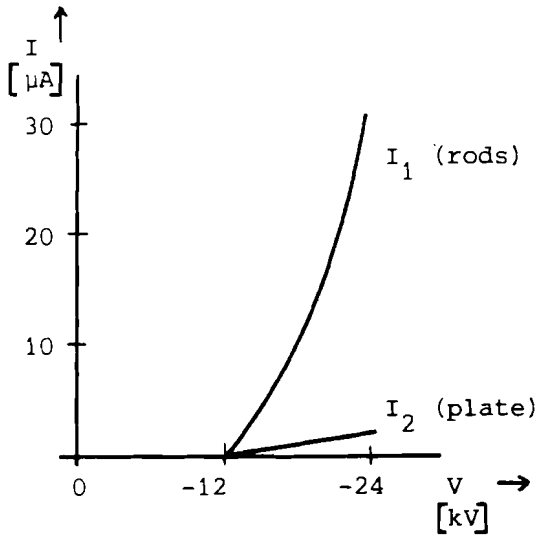

Fig. 4.2. Current versus applied voltage; S_1 = d = 30 mm and h = 60 mm.

Figure 4.3 shows schematically the different regions of corona wind generation in a point to rods configuration.

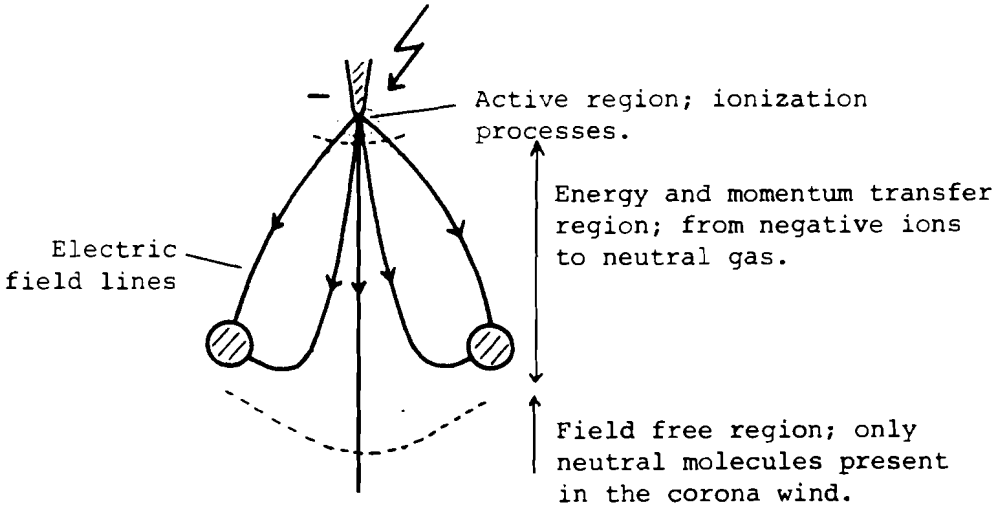

Fig. 4.3. Different regions in an electric wind system.

5. Hot-Wire Anemometry.

Anemometer measurements are based on a measurement of the convective heat loss from an electrically heated fine wire [8]. With this technique measurement of air velocities down to 0.2 ms^{-1} and turbulence frequencies up to 100 kHz are possible. In Section 5.1 the theory of the constant temperature hot-wire anemometry is presented. The Sections 5.2 and 5.3 deal with the experimental setup and the measurements respectively. In the last Section, 5.4, the obtained results are presented.

5.1. Theory.

A constant temperature anemometer consists of a wheatstone bridge and a feedback amplifier as shown in Fig. 5.1.1. The hot-wire forms one branch of the bridge and is kept at a constant temperature.

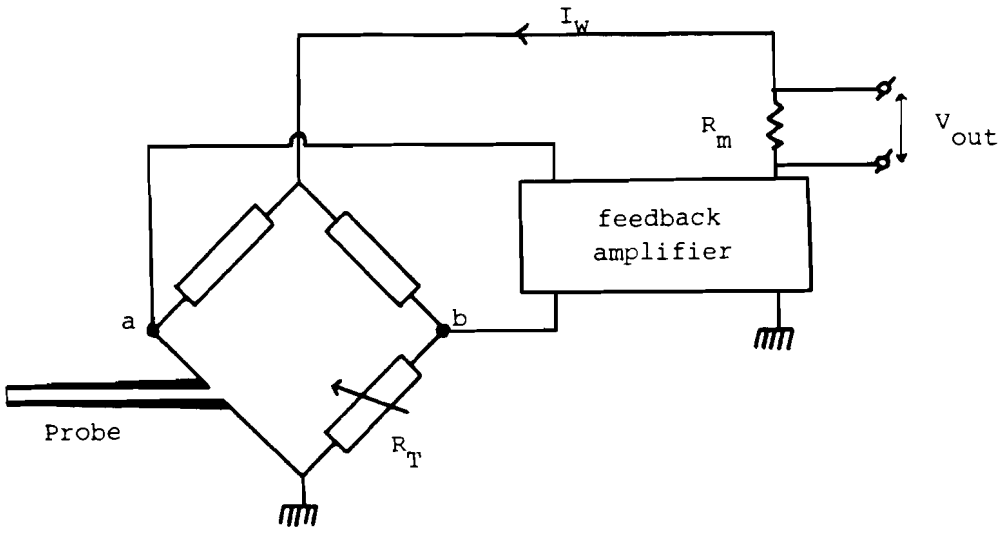

Fig. 5.1.1. Constant temperature anemometer.

The current, I_w, which flows through the hot-wire gives an electric power input $R_w I_w^2$ which heats the wire to an adjustable temperature of about 300°C. When the air flow around the sensor cools the wire the feedback amplifier increases the current I_w as a result of the bridge unbalance voltage between the points a and b. If the feedback loop is properly adjusted the temperature of the wire is kept constant. This feedback technique minimizes the effect of the thermal lag of the

wire and makes velocity measurements with turbulence frequencies up to 100 kHz possible. The instantaneous value of the electric power input, usually measured as a voltage across a resistor, is not a simple function of the velocity of the air flow. The output signal is also influenced by:

- non uniformities in temperature and flow pattern near the ends of the hot-wire.
- dirt and dust deposition on the wire.
- aging of the wire, due to prolonged operation at high temperatures.
- variation in temperature and other properties of the surrounding air.
- the angle between the wire and the mean flow direction.

For these reasons calibration of a hot-wire sensor is always necessary. Furthermore hot-wire readings are difficult to interpret because the wire is mainly sensitive to velocities in a plane perpendicular to the direction of the wire. Figure 5.1.2 shows a hot-wire probe with a 5 μm diameter tungsten wire of 2 mm length. A calibration curve for such a probe is shown in Fig. 5.1.3.

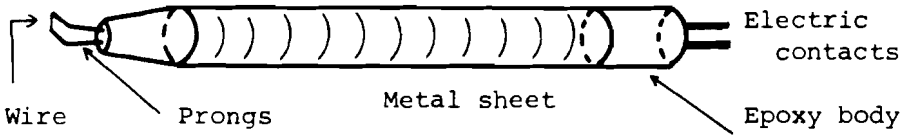

Fig. 5.1.2. Hot-wire probe.

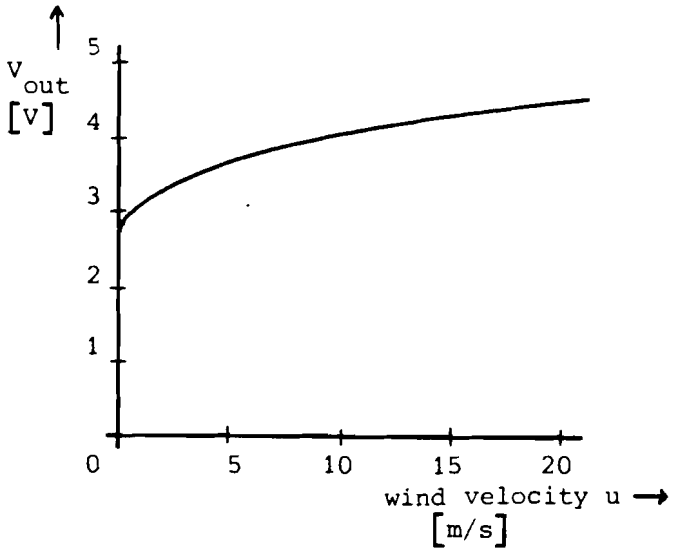

Fig. 5.1.3. Calibration curve for a hot-wire probe; curve can be fitted by: $V_{out} = 2.7 + 0.48u^{0.45}$.

5.2. Experimental Setup.

Figure 5.2.1 shows a block diagram of the experimental setup for the determination of average wind velocities and the recording of the anemometer output signal. The hot-wire probe in the electric wind system can be moved in the x, y and z direction by means of a positioning mechanism. The output signal of the anemometer unit can be fed to an x-t recorder, an oscilloscope or a d.c. voltmeter. The d.c. voltmeter measures the averaged signal of the anemometer unit as the output of an additional low pass filter.

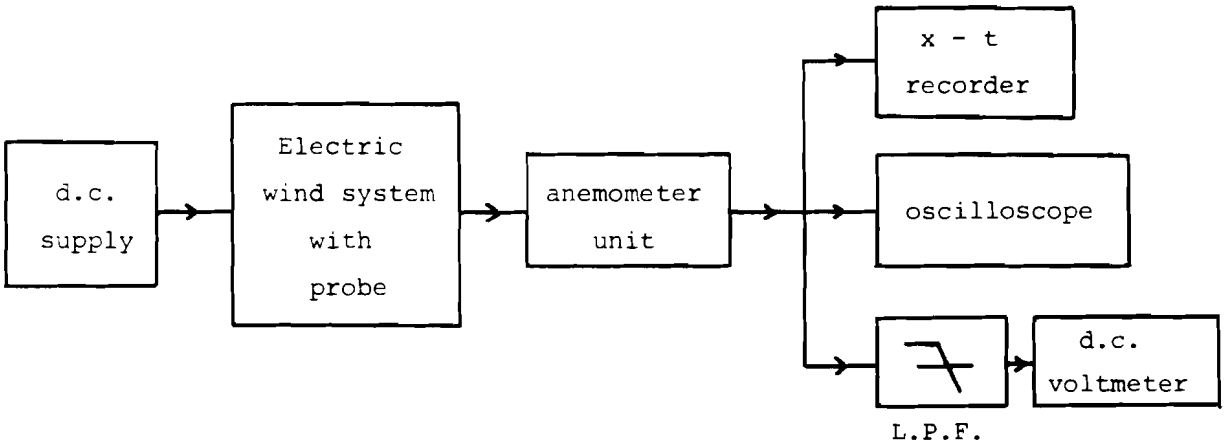

Fig. 5.2.1. Block diagram of the experimental setup.

Figure 5.2.2 shows the configuration used for the determination of the average wind velocity as a function of the voltage applied to the point. For these measurements the probe is situated right below the corona discharge point with a fixed value of h = 30 mm. This setup is also used for measuring average wind velocity profiles. The probe is then situated at a fixed value of h and the anemometer unit output signal is recorded when the position of the probe is changed in the y and z directions.

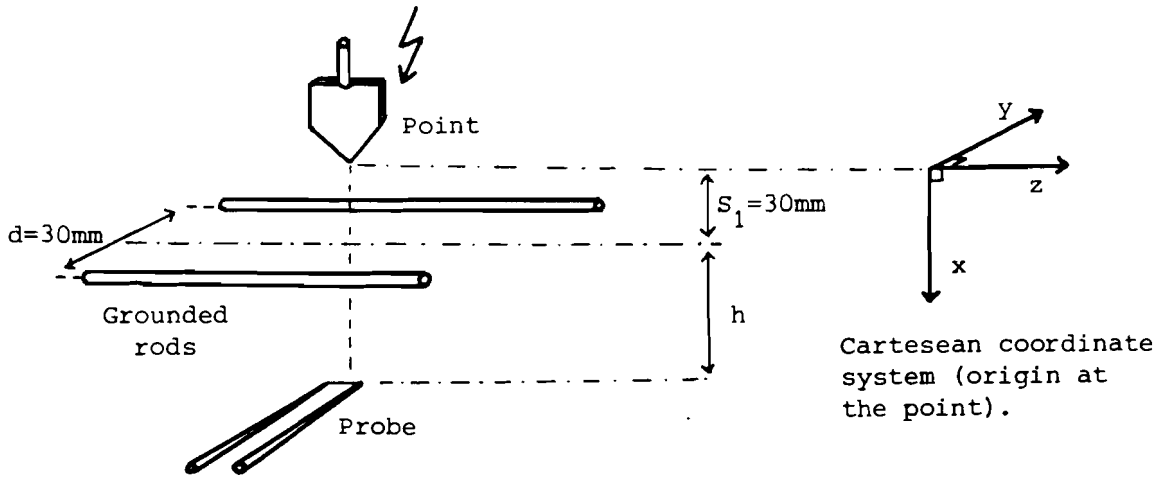

Fig. 5.2.2. Configuration for the determination of corona wind quantities.

5.3. Measurements and Results.

Figure 5.3.1 shows a plot of the average wind velocity, versus the voltage applied to the point. For voltages just above the corona onset voltage the corona discharge and thus the corona wind is very unstable. From oscilloscope pictures it turns out that the corona wind comes in bursts with irregular time intervals between them. This phenomenon was also observed during the $TiCl_4$ experiments of Chapter 7.

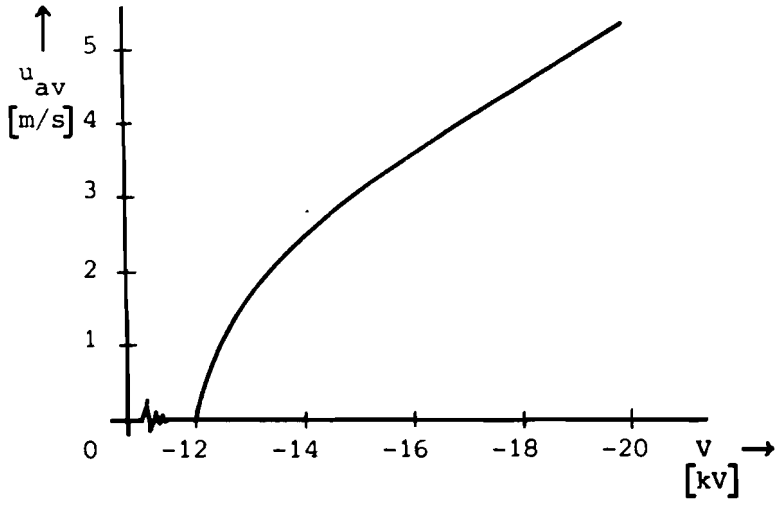

Fig. 5.3.1. Average wind velocity versus applied voltage.

The average wind velocity is roughly proportional to the applied voltage, at voltages well above the corona starting voltage:

$$u_{av} \propto V \qquad \text{for} \quad V >> V_i. \tag{5.3.1}$$

The results of Fig. 5.3.1 agree with the dependency of the average wind velocity on the corona current I_1:

$$u_{av} \propto \sqrt{I_1}, \tag{5.3.2}$$

as is reported in the literature [1]. From Eq. (4.1) we already knew:

$$I_1 = K_1 V(V-V_i), \tag{5.3.3}$$

together with Eq. (5.3.2) we get:

$$u_{av} = K_3 \sqrt{V(V-V_i)}, \tag{5.3.4}$$

where K_3 is another constant. Equation (5.3.4) is in agreement with the plot shown in Fig. 5.3.1; for values of V well above the corona onset voltage it reduces to Eq. (5.3.1). The corona wind jet has a long reach of at least 25 cm in this electric wind system and hardly widens with increasing distance h below the rods. Figure 5.3.2 shows a velocity profile for V = -16 kV and S_1 = d = h = 30 mm.
The obtained velocity profiles for a fixed value of h are bell shaped. The maximum velocity at the center decreases with increasing value of h. The velocity profiles in the z direction are similar for all h while those in the y direction are not. Furthermore the velocity profiles in the y direction are wider than those in the z direction. This together with the fact that the observed profiles in the y direction behave differently, might indicate that the jet as a whole is moving more in the y than in the z direction. A wiggling of the central core of the jet was observed in Schlieren pictures [9].

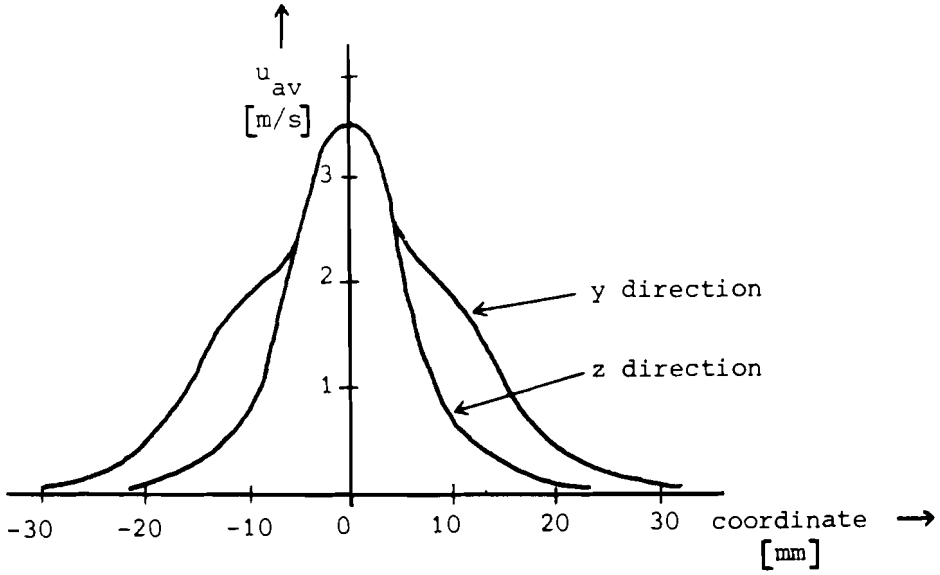

Fig. 5.3.2. Average wind velocity versus y and z coordinates; S_1 = d = h = 30 mm, V = -16 kV.

Experiments with "shielding" devices [10] show that most of the negative ions reach the grounded rods. A shielding device for the hot-wire sensor is a device that should divert charged particles away from the wire and disturb the flow field as little as possible. The experiments show no significant differences between the readings of a shielded and an unshielded hot-wire sensor for distances h greater than the rod to rod spacing d. An additional test was to measure the current drawn by an unshielded hot-wire placed at a distance less than d below the plane of the rods; even then this current was less than 0.05 μA. This confirms the result of Chapter 4 that most of the ions flow to the two grounded rods.

6. Visualization of Corona Wind

In this chapter a visualization technique is used to make the corona wind flow visible. In Section 6.1 an artificial mist, generated by solid carbon dioxide is used to make the corona wind flow pattern visible near the discharge point. Section 6.2 deals with the behaviour of mist particles in an electric wind system in order to determine if the visual flow patterns are a true representation of the corona wind flow. The experimental setup is the subject of Section 6.3 and some results are presented in Section 6.4.

6.1. Artificial Mist generated by Solid Carbon Dioxide.

Figure 6.1.1 shows the pressure vessel in which the artificial mist is generated. It contains water of approximately 60°C and on top of it is a heavy rubber membrane with a 5 mm diameter tube in it. When small lumps of solid carbon dioxide (-80°C) are put into the water the carbon dioxide immediately starts to boil. The cold CO_2 bubbles rise to the surface of the water and cool the air in the vessel. The air temperature drops below the freezing point of water and the water vapour condenses and forms a dense white mist. This mist is pushed through the tube by the pressure built up by the carbon dioxide gas. By adjusting the rubber membrane on top of the vessel is it possible to create a nearly constant pressure and thus a constant flow of mist for a few minutes. The flow velocity in the tube depends on the water temperature and the amount of solid CO_2. The flow velocity was estimated by ticking against the tube just above the rubber membrane and by measuring the time needed for the disturbance to reach the flow exit. In this manner flow velocities between 0.5 and 2 ms^{-1} were measured.

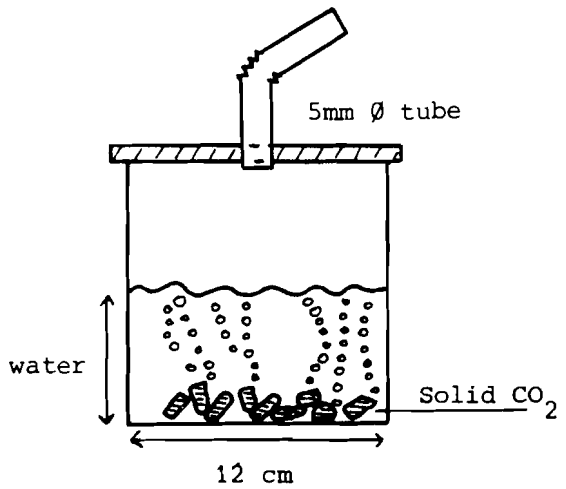

Fig. 6.1.1. Pressure vessel for artificial mist generation.

For a tube flow the Reynolds number is defined as

$$Re = \frac{u.D}{\nu} , \qquad (6.1.1)$$

u is the average flow velocity of the mist, D is the tube diameter and ν is the kinematic viscosity of air. For a flow velocity of 2 ms^{-1} and a tube diameter of 5 mm the Reynolds number is 670.
When the device shown in Fig. 6.1.2 is used to create a multi beam flow the Reynolds number is 270. For these Reynolds numbers the tube flow is still laminar since the transition to turbulence occurs only when Re > 2100.

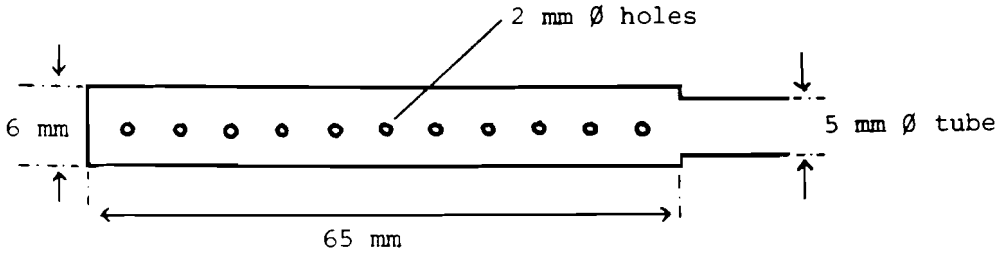

Fig. 6.1.2. Multi beam flow device.

6.2. Behaviour of Mist Particles in an Electric Wind System.

In mist of condensed water vapour particle sizes are between 5 and 100 µm. For diameters larger than 1 µm only field bombardment plays a role in a possible charging of the particles. Field bombardment means that the externally applied electrical field drives the ions towards the particle surface. The theoretical charge acquired by a spherical particle by field bombardment is expressed by [11]:

$$q_f = q_\infty \cdot \frac{t/\tau}{1 + t/\tau} \quad . \qquad (6.2.1)$$

In expression (6.2.1) q_f is the acquired charge, q_∞ is the saturation charge, τ is the charging time constant and t is the charging time. The saturation charge q_∞ and the charging time constant τ are given by:

$$q_\infty = 4\pi\varepsilon_o \cdot \frac{3\varepsilon_r}{\varepsilon_r + 2} \cdot a^2 E \qquad (6.2.2)$$

$$\tau = \frac{4\varepsilon_o E}{J} \quad . \qquad (6.2.3)$$

E is the charging field strength, a the particle radius, J the ion current density, ε_r the relative permittivity of the particle and ε_o the permittivity of vacuum. A 20 µm diameter mist particle (ε_r of water is 81) can reach a saturation charge of 1.9×10^{-14} As or 1.2×10^5 electronic charges in an electric field of 6 kV $(cm)^{-1}$. At voltages well above the corona onset voltage the following forces act on a charged particle:

1. Gravitation force

$$\vec{F}_g = m\vec{g}, \qquad (6.2.4)$$

where m is the mass of the particle and $\vec{g}$ the gravitational acceleration.

2. Electric force

$$\vec{F}_e = q_f\vec{E}, \qquad (6.2.5)$$

where q_f is the acquired charge and $\vec{E}$ the field strength.

3. Friction force

$$\vec{F}_f = 6\pi\eta a\Delta\vec{u}, \qquad (6.2.6)$$

where η is the gas viscosity, a the particle radius and $\Delta\vec{u}$ the velocity difference between the particle and the surrounding gas. The friction force as given above in Stokes law is valid if the sphere-Reynolds number is less then 10. The sphere-Reynolds number is expressed by:

$$Re_s = \frac{2a|\Delta\vec{u}|}{\nu}, \qquad (6.2.7)$$

$\Delta\vec{u}$ is the velocity difference between the particle and the surrounding gas, a the sphere radius and ν the kinematic viscosity.

4. Dipole force

$$\vec{F}_d = \nabla(\vec{p}\cdot\vec{E}), \qquad (6.2.8)$$

where $\vec{p}$ is the total dipole moment of the charged particle. The gravitation force and the dipole force are small compared to the electric force. For this reason the slow migration velocity of the particles can be obtained from the equilibrium equation:

$$\vec{F}_e = \vec{F}_f \qquad (6.2.9)$$

or

$$q_f\vec{E} = 6\pi\eta a\Delta\vec{u}. \qquad (6.2.10)$$

From Eq. (6.2.10) we obtain:

$$\Delta\vec{u} = \vec{u} - \vec{u}_o = \frac{q_f\vec{E}}{6\pi\eta a}, \qquad (6.2.11)$$

$\vec{u}$ is the velocity of the mist particles and $\vec{u}_o$ the velocity of the surrounding gas. We can characterize the motion of the mist particles by introducing the dimensionless factor K, valid for absolute values:

$$K = \frac{u}{u_o} = 1 + \frac{q_f E}{6\pi\eta a u_o}. \qquad (6.2.12)$$

If the dimensionless factor K is close to unity the mist particles move with the surrounding gas and are only little affected by the electric field. For a factor K much greater than unity the velocity of the mist particles is much greater than the gas velocity and is completely determined by the electric field. Charging of mist particles mainly occurs in the high field in the active region near the point. The gas velocity near the point is very high, up to 20 ms^{-1}. The time available for charging turns out to be small compared to the charging time constant

τ in Eq. (6.2.3). Therefore q_f remains only a fraction of the saturation charge q_∞ in Eq. (6.2.2). For a 20 μm diameter mist particle this fraction turns out to be 0.2 q_∞. In that case a K-value of 1.27 in a high field region of E = 12 kV $(cm)^{-1}$ and a gas velocity of 10 ms^{-1} is obtained. If we assume that the charge which this 20 μm diameter particle acquires in the high field region remains constant we obtain a K-value of 1.17 in a region where E = 3kV $(cm)^{-1}$ and the gas velocity 4 ms^{-1}. We see that even for a mist particle which is charged in the vicinity of the corona point the value of K is only a little more than unity. This indicates that the velocity of the mist particles is only little affected by the electric field of the corona discharge. In practice most of the mist will be injected in a low field region, therefore the effect on the gas velocity will be even less than calculated. The conclusion is that the carbon dioxide generated mist can readily be used in an electric wind system to visualize the gas flow.
Note that "filament" or "streak" lines as defined in Reference 12, are made visible with this technique.

6.3. Experimental Setup.

The experimental setup is shown in Fig. 6.3.1. In all experiments an electric wind system is used with S_1 = d = 30 mm. A SONY video camera (AVC3250CE) is used for the recording, toghether with a U-matic recorder (VO-2630) and a T.V. monitor. The camera is at 1.5 m distance from the setup while the camera angle is 30°. A microphone is used to record the parameters of the experiments on the soundtrack.

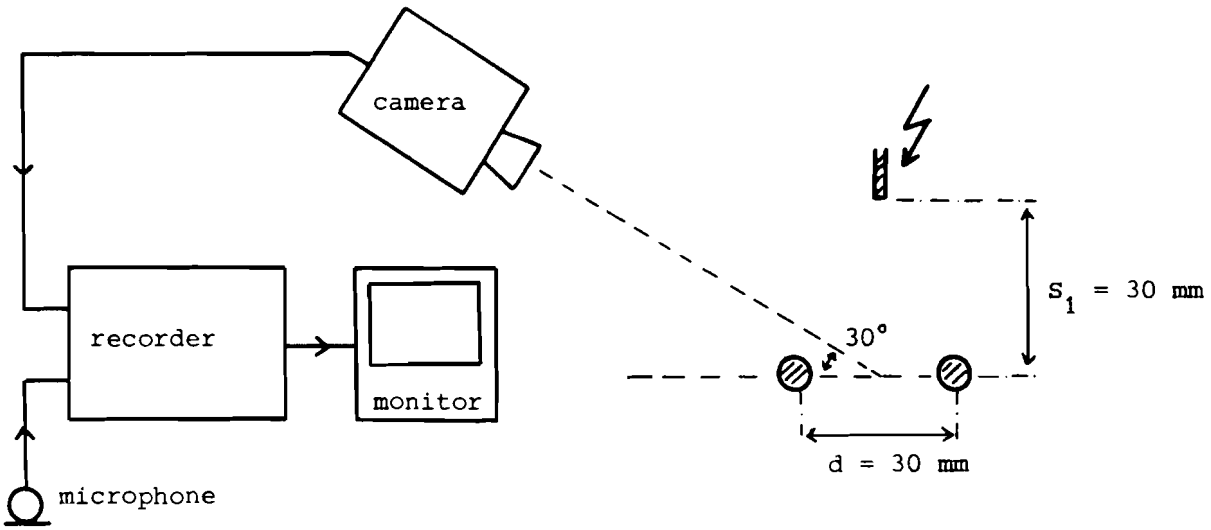

Fig. 6.3.1. Experimental setup.

The mist generated in the vessel is conducted to the point by an insulating tube of 5 mm diameter. The tube itself or the multi-beam flow device of Fig. 6.1.2 is used to introduce the mist in the setup. In order to introduce mist at the corona point a special point was constructed. It is a flat 90 degree 1 mm thick brass point with a cutout at the top to accomodate the tube. With this arrangement the white mist can flow down behind and in front of the point. In spite of our efforts to protect the setup against air currents, for instance by means of a plastic tent around it, we still had trouble with spontaneous air flow. This can be seen at several places on the video tapes and in some photographs.

6.4. Results.

The photographs 1 to 3 show pictures where the mist is introduced downward into the electric wind system by a multibeam flow device parallel to the rods. The two rods are grounded, S_1 = d = 30 mm and a voltage of -20 kV is applied to the point.

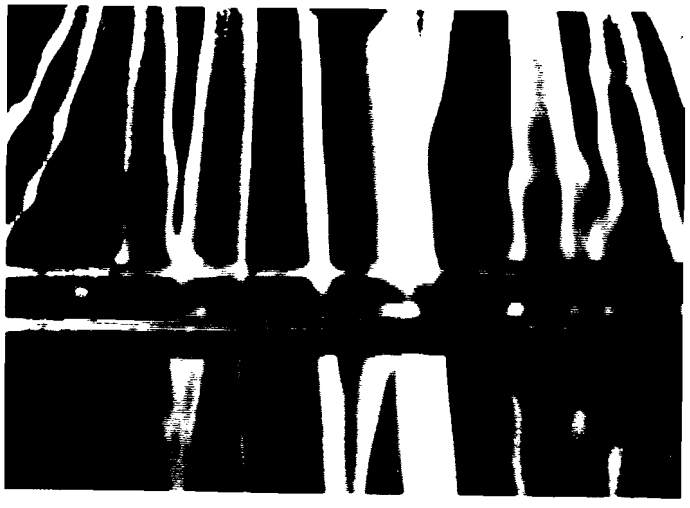

Photograph 1; no voltage applied to the point.

Photograph 2; 0.21 s after switching on -20 kV.

Photograph 3; 1.67 s after switching on -20 kV (steady state).

In about 1.5 s the flow has reached a steady state and from far left and right the gas flow is directed towards the point and then pushed down with great velocity between the rods. The diameter of the beam below the rods is approximately 35 mm. At the center, just below the point, the gas velocity has its maximum. This can be seen in the photographs because the mist is thicker at the outside than at the center of the flow. At higher gas velocities the mist becomes less dense because of the quicker flow off of the mist particles while the supply rate is still the same. Careful study of the video tape reveals that it takes generally less than 0.04 s for the flow to respond to the applied voltage and within one or two seconds a stationary flow is established. At voltages below the corona onset voltage no effects on the mist flow are observed.

7. Experiments with Titanium Tetrachloride.

In this chapter a technique is used to create thin layers of "mist" on objects which are placed below the discharge point in an electric wind sytem. The effects of the corona wind on such a layer, which simulates a stationary boundary layer, can be investigated in this manner. Section 7.1 starts with some characteristics of titanium tetrachloride. In Section 7.2 the experimental setup is described and the results of the experiments can be found in Section 7.3.

7.1. Characteristics of Titanium Tetrachloride.

Titanium tetrachloride is a colorless uninflammable liquid with a boiling point of 136°C and a mass density of 1.7×10^3 kgm^{-3}. It has a pungent odor and is vigorously hydrolyzed by water. In air $TiCl_4$ reacts with the present water vapour according to the reaction:

$$TiCl_4 + 2\ H_2O \rightarrow TiO_2 + 4\ HCl\uparrow\ . \qquad (7.1.1)$$

The formed titanium dioxide, a white powder, gives a heavy very dense white mist. The hydrochloric acid, HCl, is a poisonous pungent and very corrosive gas. Titanium tetrachloride is a liquid which spreads and wets the surface of test objects completely. On copper, brass, glass and plexiglass $TiCl_4$ can be used with success whereas "soft" plastics, iron and aluminium are attacked by it. The formed TiO_2 creates, together with the water vapour in air, a greasy deposition on the test objects. With a moist cloth most of the objects can be easily cleaned.

7.2. Experimental Setup.

The experimental setup used is the same as described in Section 6.3. Now the camera is situated 1 m from the setup with a camera angle of zero degrees. The test objects, as for instance shown in Fig. 7.2.1, are placed on a horizontal plate a distance h below the corona point.

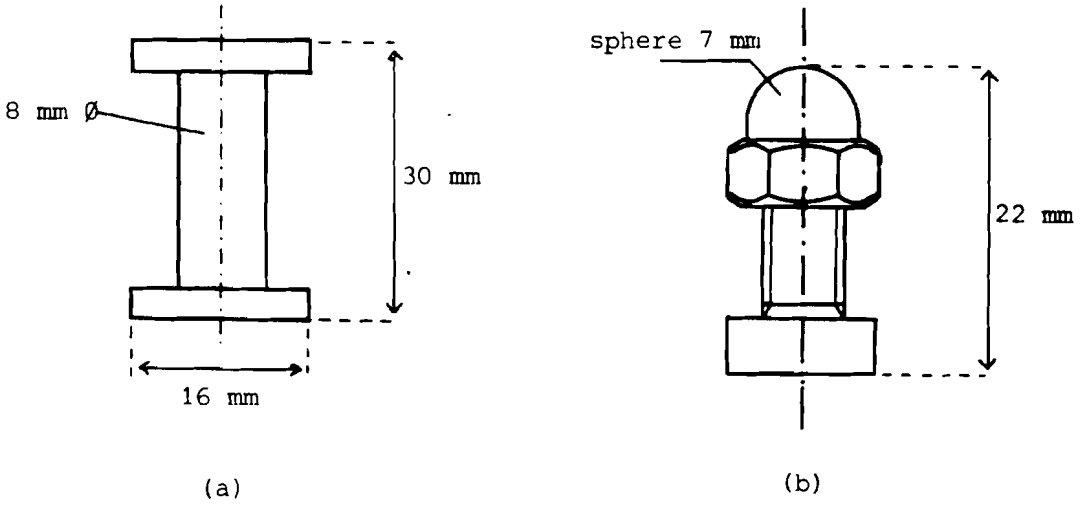

Fig. 7.2.1 Copper test objects.

7.3. Results.

The photographs 4 and 5 show two $TiCl_4$ pictures with the test object of Fig. 7.2.1 (a) placed below the corona point. The distance between the corona point and the upper surface of the test object is 55 mm with S_1 = d = 30 mm.

Photograph 4; applied voltage -12 kV, stationary flow.

Photograph 5; applied voltage -15 kV, stationary flow.

In photograph 4 the mist flows almost horizontally thus indicating that the corona wind jet has a smaller diameter than the diameter of the test object (16 mm). The video tape and the photographs show also the very fast response of the $TiCl_4$ generated mist to the applied voltage as in Chapter 6 with the artificial mist experiments. The already mentioned bursts of the corona wind at voltages a little above the corona onset voltage are also observed in these experiments. Photograph 6 shows the test object of Fig. 7.2.1 (b) during such a corona wind burst with an applied voltage of -7 kV to the discharge point. The repetition frequency of the bursts is between 0.1 and 1 Hz. .

Photograph 6; corona wind burst.

It is clearly demonstrated by these photographs and many others that the narrow corona wind jet disrupts the mist layer created by $TiCl_4$ on the test objects very rapidly and effectively.

8. Comparison of a Corona Wind Jet and an Orifice Jet.

In this chapter a comparison between a corona wind jet and a jet originating from an orifice is made. A difficulty in the comparison between the two jets is the question which parameter should be the same in both jets. Figure 8.1 shows a sketch of a corona wind jet and an orifice jet.

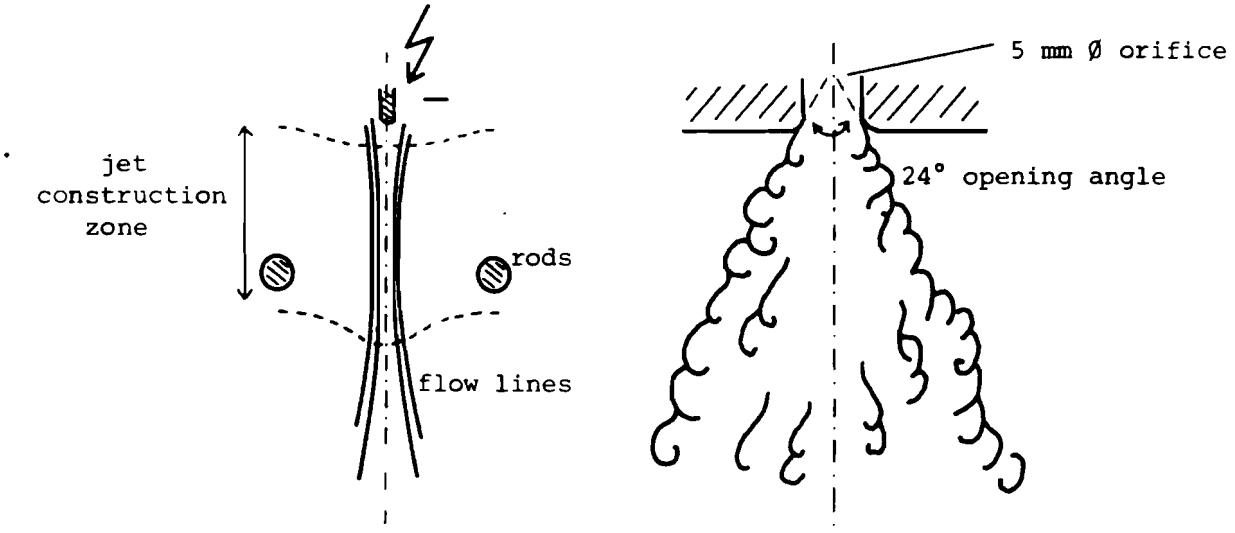

Fig. 8.1. Corona wind jet and orifice jet.

The orifice jet theoretically becomes turbulent when the Reynolds number is greater than 2100 but in practice laminar free jets originating from an orifice cannot be produced [12]. The edge of the orifice introduces disturbances that grow and eventually make the jet a turbulent one. In Fig. 8.2 the growth of the disturbances introduced at the edge of an orifice is shown.

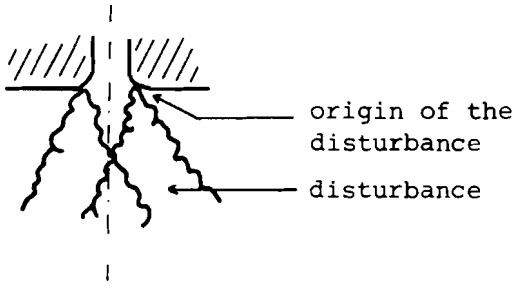

Fig. 8.2. Growth of the disturbances in an orifice jet.

Free jets are therefore always turbulent regardless of the velocity and the shape and diameter of the orifice. The jets have a bell shaped velocity profile and the maximum gas velocity decays inversely with the distance along the jet. The opening angle of the jet is about 24 degrees [13]. The forces which stabilize the jet cease to work when the jet leaves the flow opening; from this moment on the jet can only decay. Furthermore the transition from pipe flow to free jet is very abrupt and the disturbances introduced as "initial conditions" also degenerate the free jet.

The corona wind jet originates in the region surrounding the corona discharge point and has a large zone as shown in Fig. 8.1 in which the jet is formed and accelerated by the rapidly drifting ions. It can be smoothly formed in the time needed by the jet to travel the distance between the point and the grounded rods with a stable velocity profile. When the jet leaves the energy input zone the change to free jet is not abrupt as in the case of an orifice jet but very gradual. For this reason it has a much better chance to create a laminar free jet. Indications for the existence of a laminar free jet are the photographs given in this report and the small cross section of the jet. When the jet has travelled past the grounded rods the maximum velocity decays as in a free jet but the bell shaped velocity profile spreads much less than in a free jet

originating from an orifice. The conclusion is that in an electric wind system the jet can be "better" generated than in the case of an orifice jet. The electric wind system acts as a special nozzle which creates a free jet with a laminar character, and so a greater range and a more directed motion than in a jet originating from an orifice are possible.

9. Discussion and Conclusions.

The corona wind can be investigated with a hot-wire anemometer and can be visualized by means of a solid carbon dioxide generated mist. The experiments show that the corona wind jet generated in an electric wind system is more laminar, spreads less and has a longer reach than a jet originating from an orifice. The reason for this is that the smoothly distributed body force acting in the corona wind generates much less initial disturbance than the edge of an orifice in the case of an orifice jet. The negative ions cannot contribute significantly to the heat transfer since very few ions reach the heat transfer surface; almost all ions are collected by the grounded rods.

This is confirmed by the anemometer measurements where the probes collected no measurable current when they were placed a distance h, larger than d, below the plane of the rods.

The conclusion must be that the enhancement of heat transfer is caused by the more laminar character and the longer reach of the directed motion of the corona wind jet.

The outcome of this study is in general agreement with earlier studies with Schlieren diagnostics [9] and electrical measurements [7]. A summarizing report is Reference 14.

REFERENCES

(1) Robinson, M., Movement of air in the electric wind of the corona discharge, AIEE Trans., 114, pp. 143-150 (1961).

(2) Mitchel, A.S. and L.E. Williams, Heat transfer by the corona wind impinging on a flat surface, J. Electrostatics, 5, pp. 309-324 (1978).

(3) Goldman, M. and A. Goldman, Corona discharges in "Gaseous Electronics Vol. I", M.N. Hirch and H.J. Oskam (editors), Academic Press (1978).

(4) Stuetzer, O.M., Ion drag pressure generation, J. Appl. Phys., 30, pp. 984-994 (1959).

(5) Kulacki, F.A., Electrohydrodynamic enhancement of convective heat and mass transfer in "Advances in transport processes", A.S. Mujumdar and R.A. Mashelkar (editors), Wiley Eastern Limited (1982).

(6) Lama, W.L. and C.F. Gallo, Systematic study of the electrical characteristics of the "Trichel" current pulses from negative needle-to-plane coronas, J. Appl. Phys., 45, pp. 103-113 (1974).

(7) Kadete, H., Negative corona current characteristics of an electric wind system, EHO MEMO 84/26 (February 1984).

(8) Bradshaw, P., Chapter 5 in "An introduction to turbulence and its measurements", Pergamon Press (1971).

(9) Kadete, H., Schlieren measurements on corona wind, EHO MEMO 84/28 (August 1984).

(10) Vaessen, P.T.M., Hot-wire anemometer study of the electrical wind in an electric wind system, EHO MEMO 84/36 (December 1984).

(11) Masuda, S., Recent progress in electrostatic precipitation, 4th. conf. on static electrification, London 5-8 May 1975, The Institute of Physics Conference Series no. 27, pp. 154-171 (1975).

(12) Tritton, D.J., Chapter 11 in "Physical fluid dynamics", Van Nostrand Reinhold Company (1977).

(13) Rajaratnam, N., Chapter 2 in "Turbulent jets", Elseviers Scientific Publishing Company (1976).

(14) Kadete, H., P.T.M. Vaessen and P.C.T. van der Laan, Enhancement of heat transfer by corona wind, To be published in the proceedings of the 7th. International Symposium on Plasma Chemistry, Eindhoven July 1-5 (1985).

EHO MEMOS are internal reports of the High Voltage Group of the Eindhoven University of Technology.

ACKNOWLEDGMENT

This study is a continuation of research carried out by mr. H. Kadete of the University of Dar es Salaam, Tanzania. A summarizing publication on this cooperation is Reference 14.
I gratefully acknowledge the enthusiastic technical support by mr. P.F.M. Gulickx. I am also grateful for the technical assistance given by mr. N. Gijsbers with the video work.
Finaly I would like to thank mrs. R. Blatter for typing the manuscript.